An X-Band Linear-to-Circular Polarizer With High Refractive-Index Metamaterials

YAT SING TO [1] (Graduate Student Member, IEEE), XUE REN [2] (Member, IEEE), QUAN-WEI LIN [1] (Member, IEEE), AND HANG WONG [1] (Senior Member, IEEE)

[1] State Key Laboratory of Terahertz and Millimeter Waves, Department of Electronic Engineering, City University of Hong Kong, Hong Kong
[2] College of Electronics and Information Engineering, Shenzhen University, Shenzhen 518060, China

CORRESPONDING AUTHOR: H. WONG (e-mail: hang.wong@cityu.edu.hk)

ABSTRACT This paper presents a novel wideband low-profile linear-to-circular polarizer based on high refractive-index metamaterials in the X band. The proposed design is a multilayer structure that is built from two kinds of metamaterial unit cells consisting of 4-H-shaped strips and 1-H-shaped strips. Combining the two unit cells realizes the flexible and independent control of the refractive index difference between two orthogonal E-field components and thus achieves a consistent 90-degree phase delay over a wide bandwidth. Moreover, the proposed unit cell shows a high refractive index, which contributes to lowering the height of the LP-CP polarizer. In order to improve the axial ratio (AR) bandwidth, two impedance-matching layers are introduced to combat the reflection loss on the metamaterial-air boundary. Nevertheless, the proposed design can provide a wide 3 dB AR bandwidth of 37.7% and a low insertion loss of 0.5 dB with a thin profile of 0.21 λ_0. The prototype was fabricated and measured, while the experimental results agree well with the simulated ones, thus validating the working mechanism and its practical feasibility.

INDEX TERMS Circular polarization, polarization conversion, polarizer, metamaterial, refractive index.

I. INTRODUCTION

CIRCULARLY-POLARIZED (CP) wave possesses the distinguished advantages of strong anti-interference ability, and low polarization mismatching from multipath fading compared with linearly-polarized (LP) wave. They make CP waves widely used in satellite communication systems, navigation systems [1], imaging systems [2], polarization diversity of radar systems [3], and so on. For radar systems, CP waves can be used to distinguish the transmitted and received waves. For example. the left-hand circularly polarized (LHCP) incident wave reflects right-hand circularly polarized (RHCP) from the target. For the earth stations, CP antennas can allow for receiving the incoming LP wave with all angles of the polarization vector.

LP-CP polarizer is the commonly used method to generate CP wave from LP incident wave. The basic working principle is to decompose the LP incident wave into two orthogonal components with nearly equal magnitude and 90° phase difference such that a CP wave can be generated. In the last decades, various approaches have been reported to realize and analyze circular polarizers. Among them, the dielectric polarizer utilizing the anisotropy of the complex material has been reported in the literature [4], [5]. The dielectric material approach yields good radiation performance in the aspect of the wide axial ratio and stable radiation pattern across the bandwidth, but it lacks independent manipulation on the orthogonal components of the LP incident wave and results in a high profile of the polarizer itself.

Recently, approaches of 3D metamaterial unit cells have been found effective in controlling two orthogonal components of incident wave [6], [7], [8]. The proposed work in [7] combines the dielectric-air slabs with the split ring patterns to realize the 90-degree electrical path delay of the transmitting wave. In [8], a metamaterial-based partially reflected surface

(PRS) and high-impedance surface in a Fabry-Perot (FP) cavity antenna allows the independent magnitude and phase control of the transmissive wave and the reflective wave. Although the 3D unit cell-based polarizer can achieve a wide AR bandwidth with a low insertion loss, it brings a high-profile (almost one-half wavelength) structure and complexity to the antenna.

Alternatively, the 2D metasurfaces employed with the anisotropic characteristics have been investigated as polarizers extensively [9], [10], [11], [12], [13], [14], [15], [16], [17], [18], [19], [20], [21]. Meander-line polarizer report in [9], [10], [11], [12], [13], [14] is composed of dielectric slabs with metallic meandering lines printed on both sides of the slabs. Design equations of the meander-line polarizers [10], [11], [12], [13] and circuit analysis [14] have been reported. Although the design procedure of this type of polarizer is simple, the structure of the polarizer requires multiple dielectric slabs to build which leads to a very high thickness for the overall antenna body. Another approach to realizing a circular polarizer is to use frequency selective surfaces (FSS) [11], [15], [16], [17], [18], [19], [20], [21]. In [15], a single-layer FSS polarizer composed of split-slot-rings (SSRs) unit cells was proposed to convert the 45° LP wave to a CP wave. The gaps of the outer and inner SSR are placed in two orthogonal axes and optimized to generate the CP wave. It can realize a reasonable axial ratio (AR) bandwidth of 11.75% with an insertion loss of 3 dB. A dual-layer polarizer composed of a modified Jerusalem cross (MJC) FSS unit was proposed to reduce the insertion loss within the AR bandwidth [16]. By inserting a one-quarter wavelength spacer into the two metallic MJC patterns, the matching for the wave between the polarizer and the air can be improved. However, the high Q-factor structure results in a narrow AR bandwidth of 10% for the polarizer, which limits applications to recent wideband wireless systems. Furthermore, cascading layers with a spacer is a simple way to improve the AR bandwidth by reducing the Q-factor of the polarizers [11], [18], [19], [20], [21]. As reported in [20], a four-layer FSS polarizer based on a cross-shaped composition structure can realize a wide 3-dB AR bandwidth of 64%. However, the peak insertion loss reaches 2 dB. This indicates that a tradeoff among AR bandwidth, structural simplicity, polarization purity, and insertion loss exists in designing the multilayered polarizers.

In this paper, we are going to present a new structure of a low-profile polarizer for linear-to-circular polarized wave (LP-CP) conversion based on high refractive-index metamaterials. The proposed polarizer is composed of a new metamaterial combining of orthogonal H-shaped metallic strip pattern, which offers more degree of freedom than [22] in the manipulation of refractive index variations for two orthogonally polarized incident waves. By simply tuning the length of the metallic strip line pattern along two orthogonal polarizations, a 90° phase difference can be achieved. On the other hand, two impedance matching layers (IMLs) are introduced to make the amplitudes of the two
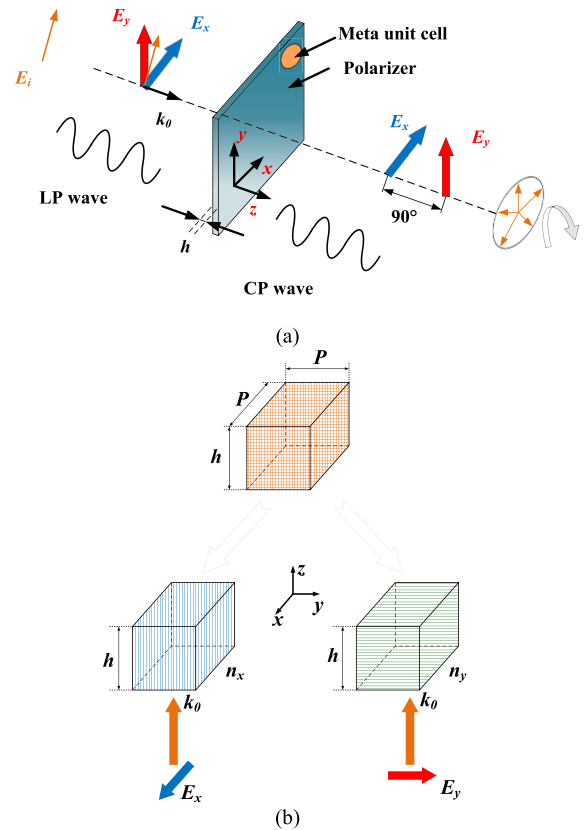
FIGURE 1. (a) General behavior of the LP-CP polarizer excited by the 45° LP incident plane wave. (b) Diagram of the anisotropic metamaterial excited with E_x and E_y.

orthogonal-polarization waves nearly equal, which meets the requirement of generating a CP wave. The proposed design is an attempt to design the polarizer by extracting the refractive index of the subwavelength anisotropic metamaterial. To validate the design, the proposed meta unit cell is analyzed with a full-wave simulator in periodic boundary conditions. The results show that the proposed polarizer exhibits a 3-dB AR bandwidth of 42% and an insertion loss of 1 dB across the AR bandwidth for its thin structure of 0.21 λ_0.

This paper is organized as follows. Section II introduces the design methodology of the high refractive index metamaterial-based polarizer. In Section III, the design and performance of the polarizer will be presented. The refractive indexes for the core layer and IMLs in x- and y-directions are simulated and extracted to analyze the working mechanism of the proposed polarizer. A prototype was fabricated and measured to validate the performance in Section IV. A conclusion is drawn in Section V.

II. DESIGN METHODOLOGY OF WIDEBAND LP-CP POLARIZER
A. PRINCIPLE OF THE WIDEBAND LP-CP TRANSFORMATION

Fig. 1 (a) shows the working principle of the polarizer based on the meta unit cell. The incident wave E_i with 45° polarization can be decomposed into two components
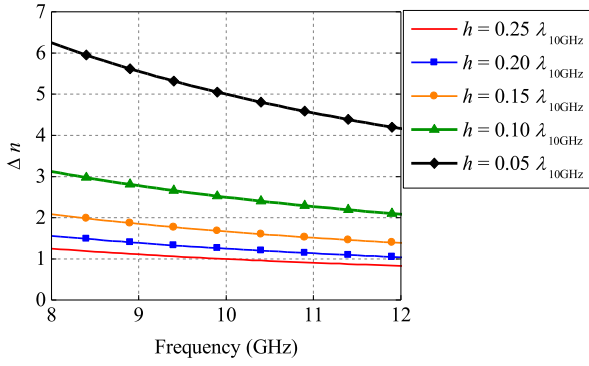
FIGURE 2. Calculated refractive index differences versus frequencies for different heights of the converter.

(a)

(b)

FIGURE 3. Configuration of (a) four H-shaped strip unit cell (UC-Y) and (b) one H-shaped strip unit cell (UC-X).

TABLE 1. Parameters for proposed four/one H-shaped strip unit cell.

Parameters	P	S_c	L_{c1}	L_{c2}	W_{c1}	h_{c1}	h_{c2}
Value (mm)	4	0.45	2.95	0.55	0.2	0.254	0.508
Parameters	W_{c2}	L_{m1}	L_{m2}	W_{m1}	W_{m2}	h_{m1}	
Value (mm)	0.45	3.1	0.55	0.2	0.4	1.016	

with orthogonal polarizations E_x and E_y. As shown in Fig. 1 (b), since the anisotropic metamaterial possesses different refractive indexes in two orthogonal polarizations, phase difference occurs when the wave goes through the anisotropic material. The phase difference $\Delta\varphi$ between the two orthogonal polarizations is calculated below,
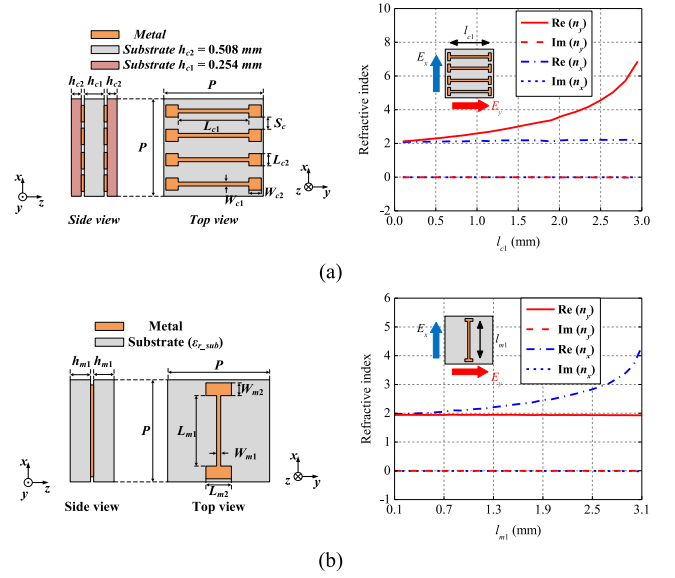
$$\Delta\varphi = |n_x - n_y| 360° \frac{h}{\lambda_0} = \Delta n 360° \frac{h}{\lambda_0} \qquad (1)$$

where n_x and n_y represent the effective refractive indexes for the two components Ex and Ey propagating through the metamaterial respectively, Δn is the difference of n_x and n_y, h is the height of the metamaterial, and λ_0 is the wavelength at working frequency. In order to fulfill the requirement for the generation of a CP wave, the phase difference between the two polarization $\Delta\varphi$ is set as 90°.

The calculated refractive index differences at 8 GHz–12 GHz are derived from (1) as shown in Fig. 2 by fixing the phase difference $\Delta\varphi$ as 90°. As can be seen, for a given height of the polarizer, the refractive index difference $\Delta n = n_y - n_x$ is inversely proportional to the height of the polarizer h/λ_0, while it varies decreasingly over the increasing frequency range. The relationships retrieved from Fig. 2 implied that the wideband and low-profile polarizer design required a high refractive index difference and rapid variation, and thus to maintain the phase difference between orthogonal polarizations $\Delta\varphi = 90°$ over the frequency range. The calculated results will give a guideline for establishing a wideband polarizer.

B. INDEPENDENT PHASE CONTROL OF ORTHOGONAL POLARIZED COMPONENTS

To realize the independent path delay control of the orthogonal components, the proposed anisotropic meta unit cell employed one H-shaped strip pattern (UC-X) and four H-shaped strip patterns (UC-Y) along the x- and y-axis respectively, as shown in Fig. 3. Succeeding the design proposed in [22], the unit cell design in four H-shaped strips (UC-Y) provides a large variation of the refractive index along the y-axis by varying the length of the horizontal arm length as depicted in Fig. 3 (a). However, it limited

variation of the x-axis refractive index due to the insufficient changes in the vertical arm's length. Thus, the unit cell design with an additional vertical H-shaped strip (UC-X) is introduced to offer another degree of freedom in varying the x-axis refractive index as shown in Fig. 3 (b), and thus to realize the CP wave with independent control of the orthogonally polarized components. Considering UC-X for x-polarized wave, one H-shaped metallic strip is sandwiched with two substrates *Rogers 4003C* with $\varepsilon_{r_{sub}} = 3.38$, $h_{m1} = 1.016mm$. Meanwhile, for UC-Y in y-polarization, four H-shaped metallic strips are symmetrically attached on both sides of a dielectric substrate *Rogers 4003C* with $\varepsilon_{r_{sub}} = 3.38$, $h_{c1} = 0.508mm$ that is sandwiched between two substrates *Rogers 4003C* with $\varepsilon_{r_{sub}} = 3.38$, $h_{c2} = 0.254mm$. Detailed parameters are provided in Table 1.
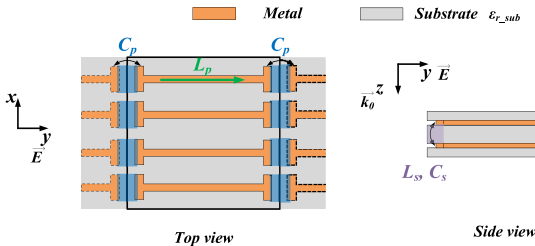
The relationship between the number of H-shaped pattern repetitions and the refractive index difference of the orthogonal polarizations is investigated through the simulation of the meta unit cell with different H-shaped pattern repetitions as depicted in Fig. 4. Throughout the ascending repetitions of the H-shaped pattern, the refractive index on y-polarizations $Re(n_y)$ is gradually increased from 4.38 to 6.99 at the operating frequency of 10 GHz as shown in Fig. 5(a), while the increment of that on x-polarizations $Re(n_x)$ is insignificant ranging from 1.95 to 2.25 as shown in Fig. 5(b). Such a phenomenon implies the refractive index difference
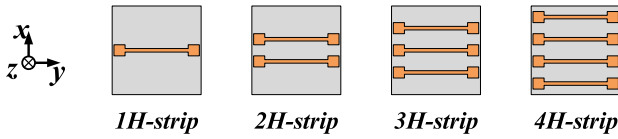
FIGURE 4. Configuration of the proposed core layer unit cell with different H-shaped pattern repetitions.
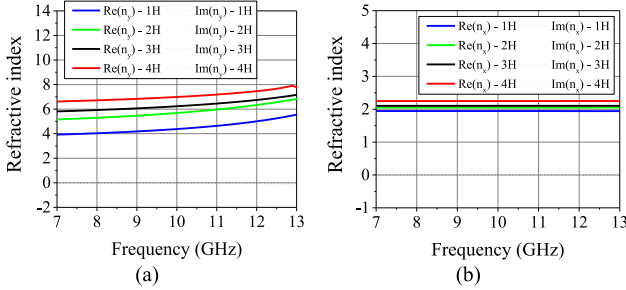
FIGURE 5. Refractive indexes of the meta unit cell with different H-shaped pattern repetitions in (a) y-pol.arizations and (b) x-polarization.

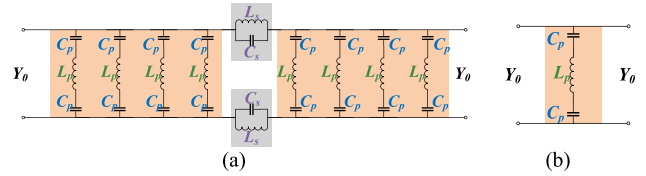FIGURE 6. Equivalent analysis of the H-shaped strip unit cell.

FIGURE 7. Equivalent model of the proposed meta unit cell (a) UC-Y (b) UC-X.

FIGURE 8. Scattering response of (a) four H-shaped strip unit cell (UC-Y) and (b) one H-shaped strip unit cell (UC-X) under circuit and full wave simulator.

TABLE 2. Evaluated equivalent circuits for UC-Y and UC-X.

Parameters	L_p	C_p	L_s	C_s
UC-Y	0.34 nH	91.4 fF	0.57 nH	109 fF
UC-X	1.25 nH	204 fF	N/A	N/A

TABLE 3. Evaluated equivalent circuits for UC-Y in the variation of L_{c1}.

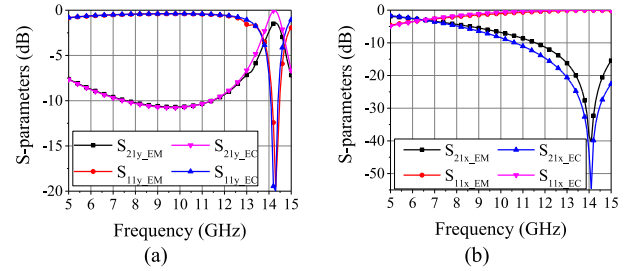| L_{c1} (mm)	L_p (nH)	C_p (fF)	L_s (nH)	C_s (fF)
1.75	0.19	23	0.39	109
2.15	0.25	31.5	0.45	109
2.55	0.30	48.8	0.52	109
2.95	0.34	91.4	0.57	109

of the orthogonal polarization is in direct proportion to the repetitions of the H-shaped pattern. To achieve the largest refractive index difference between the orthogonal polarizations, the four H-shaped strips (UC-Y) and one H-shaped strip (UC-X) are chosen to provide the maximum and minimum refractive index on y- and x-polarization respectively.

The equivalent analysis of the UC-Y and UC-X are illustrated in Fig. 6, when the unit cells are excited with the incident wave propagating along the z-axis, the incident electric field induces currents on the parallel arm of the H-shaped strip pattern, which is represented by the inductance L_p. As the electrical charges are accumulated on the vertical arms between the H-shaped strip and its neighbor unit cells in the y-axis, the capacitance C_p is considered. Especially for UC-Y, the inter-layer inductance L_s and capacitance C_s are also introduced due to the coupling within the substrate.

As a result, the equivalent circuit model of UC-Y and UC-X are evaluated in the Advanced Design System (ADS) as shown in Fig. 7. In the proposed work, the equivalent circuits for UC-Y and UC-X are listed with their corresponding values in Table 2. To validate the equivalent circuit, the scattering responses obtained from ADS, S_{11x_EC}, S_{11y_EC}, S_{21x_EC}, S_{21y_EC}, are compared with that from full wave

simulator HFSS, S_{11x_EM}, S_{11y_EM}, S_{21x_EM}, S_{21y_EM} as illustrated in Fig. 8, and thus the results made a good agreement with each other. The equivalent circuit analysis of the UC-Y in the variation of L_{c1} is demonstrated in Fig. 9 as the coupling of currents to the adjacent cell and the interlayer induction is mainly contributed by the parameters L_{c1}, thus providing significant changes in the equivalent circuit values among the dimensions of the structure. The effect of the physical dimension L_{c1} on the equivalent circuit is summarized in Table 3. As the horizontal arm length L_{c1} of the H-shaped strip is reduced, there is a significant reduction of the capacitance C_p due to the distance between the vertical arms of the H-shaped strip and its adjacent cells is increased, and thus the coupling effect between the unit cells weakens. Meanwhile, regarding the four H-shaped strips printed on both sides of the substrate as 4 pairs of parallel wires, the inductance L_p and L_s are reduced as the decrease of wire length. The capacitance C_s remains the same over the variation of L_{c1} as the substrate thickness is unchanged.
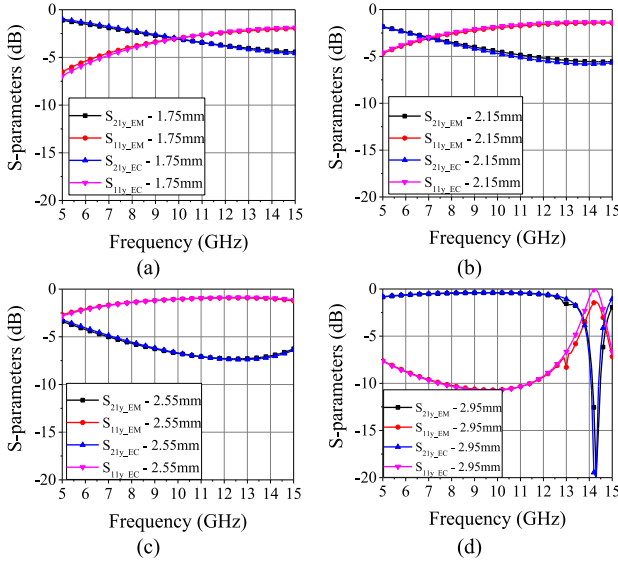
FIGURE 9. S-parameter response of four H-shaped strip unit cell (UC-Y) with L_{c1} (a) 1.75mm (b) 2.15mm (c) 2.55mm (d) 2.95mm under the circuit and full wave simulator.

FIGURE 10. Schematic diagram of LP-CP polarizer with impedance matching layer (IML).

FIGURE 11. Configuration of the proposed multilayered wideband LP-CP polarizer.

C. REDUCTION OF INSERTION LOSS

Consider the wave impedance of the proposed non-magnetic metamaterial with the refractive index of n in this work ($\mu_r = 1$),

$$\eta = \frac{\sqrt{\mu_0 \mu_r}}{\sqrt{\varepsilon_0 \varepsilon_r}} = \frac{\eta_0}{\sqrt{\varepsilon_r}} = \frac{\eta_0}{n} \qquad (2)$$
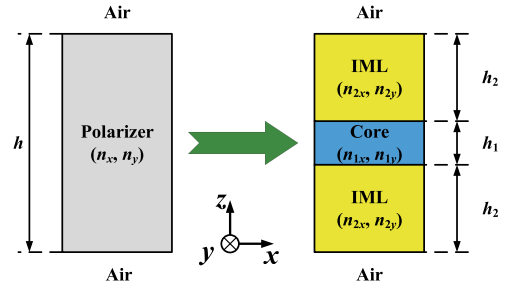
where μ_r is the relative permeability, ε_r is the relative permittivity, $\eta_0 = \sqrt{\mu_0/\varepsilon_0}$ is the wave impedance in the free space. As observed in (2), the wave impedance decreases as the refractive index increases. The different wave impedances between the metamaterial and the free space can result in the mismatching issue. Hence, it can increase the insertion loss and unbalanced magnitudes for two polarizations which will degrade the performance of CP radiation.

Therefore, impedance matching layers (IMLs) between the polarizer and the air are introduced to compensate for the loss due to the mismatching as shown in Fig. 10. To achieve the impedance matching, h_2 is selected as a quarter wavelength in IML. The wave impedance of IML is meant to be the geometrical mean of the air and the core layer, which leads to
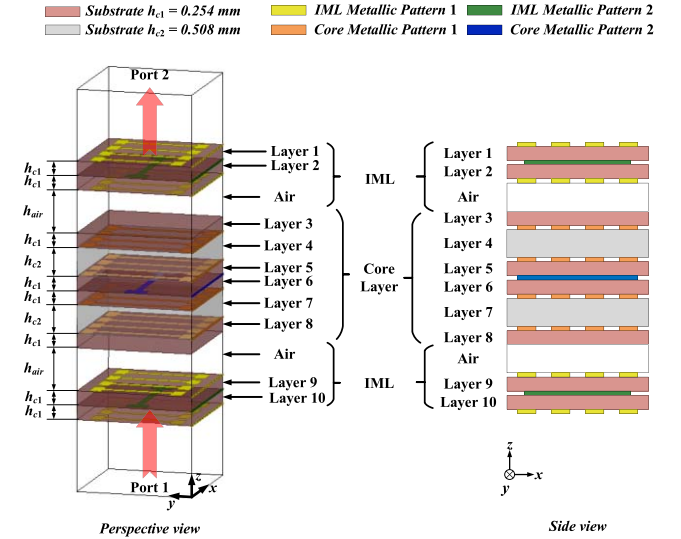
$$\begin{cases} n_{2y} = \sqrt{n_{1y}} \\ n_{2x} = \sqrt{n_{1x}} \end{cases} \qquad (3)$$

where n_{1x}, n_{1y} are the core layer refractive indexes and n_{2x}, n_{2y} are the IML refractive indexes Following the schematic diagram of the proposed polarizer as shown in Fig. 10, the relationship between the thickness of the core layer and that of the IML (denoted as h_1 and h_2) in terms of the corresponding refractive indexes n_{1x}, n_{1y}, n_{2x}, and n_{2y} is derived as follows,

$$\begin{cases} 2 \cdot n_{2y} \cdot h_2 + n_{1y} \cdot h_1 = n_y \cdot h \\ 2 \cdot n_{2x} \cdot h_2 + n_{1x} \cdot h_1 = n_x \cdot h \end{cases} \qquad (4)$$

where h is the overall thickness and n_y, n_x the refractive indexes of the polarizer in orthogonal polarization. According to (4), the height of the core layer h_1 and IML layer h_2 can be obtained with the corresponding refractive indexes n_{1x}, n_{1y}, n_{2x}, and n_{2y} to achieve the phase difference as 90°.

III. DESIGN OF HIGH REFRACTIVE INDEX-BASED LP-CP POLARIZER

The meta unit cell for the polarizer is shown in Fig. 11. The unit cell is composed of ten layers of substrates printed on four kinds of patterns. Layers 3 to 8 form the core layer. Layer 1, 2, and air gaps compose an IML while Layer 9, 10, and air gaps compose another IML. The substrates are chosen as *Rogers RO4003C* ($\varepsilon_r = 3.55$, $\tan\delta = 0.0027$) with thicknesses of 0.254 mm and 0.508 mm for consolidating the multilayer structure. The detailed design and performance of the layers will be discussed in the following sections.
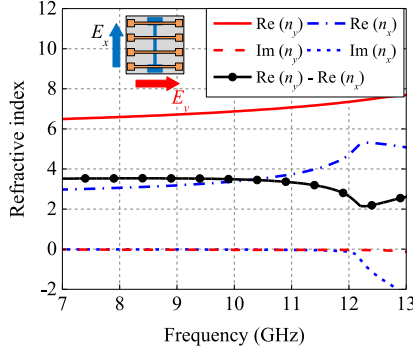
A. CORE LAYER DESIGN AND ANALYSIS

Combining the UC-X and UC-Y introduced in Section III-B, the anisotropic meta unit cell structure UC1 is proposed for constructing the core layer of the polarizer, as shown in Fig. 12. The core layer unit cell is composed of 6 layers
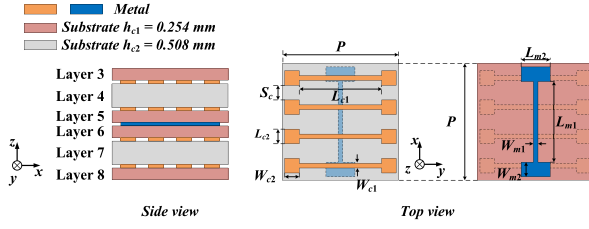
FIGURE 12. Configuration of the core layer for the proposed anisotropic meta unit cell (UC1). The parameters are $P = 4$, $S_c = 0.45$, $L_{c1} = 2.95$, $L_{c2} = 0.55$, $W_{c1} = 0.2$, $W_{c2} = 0.45$, $L_{m1} = 3.1$, $L_{m2} = 0.65$, $W_{m1} = 0.2$, $W_{m2} = 0.4$ (All are in mm).

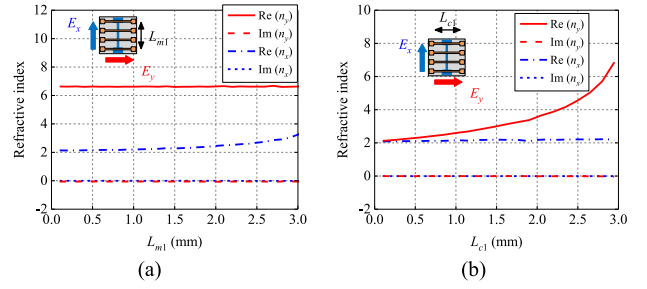FIGURE 14. Simulated refractive indexes of UC1 for different values of (a) L_{m1} and (b) L_{c1}.

FIGURE 13. Simulated refractive indexes for UC1 in two orthogonal polarizations.

FIGURE 15. Configuration of the IML for the proposed anisotropic meta unit cell (UC2). The parameters are $P = 4$, $S_a = 0.45$, $L_{a1} = 2.6$, $L_{a2} = 0.55$, $W_{a1} = 0.2$, $W_{a2} = 0.45$, $L_{n1} = 2.9$, $L_{n2} = 0.65$, $W_{n1} = 0.2$, $W_{n2} = 0.4$ (All are in mm).
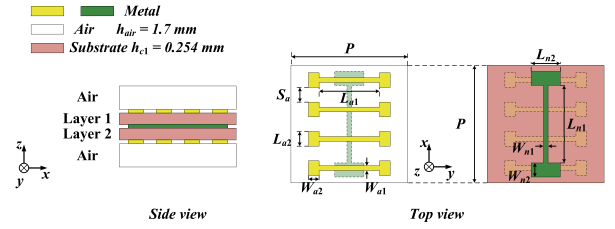
TABLE 4. Parameters for proposed wideband LP-CP polarizer.

Parameters	P	S_a	L_{a1}	L_{a2}	W_{a1}	W_{a2}	L_{n1}	L_{n2}
Value (mm)	4	0.45	2.2	055	0.2	0.45	2.75	0.65
Parameters	W_{n1}	W_{n2}	S_c	L_{c1}	L_{c2}	W_{c1}	W_{c2}	L_{m1}
Value (mm)	0.2	0.4	0.45	2.95	0.55	0.2	0.45	3
Parameters	L_{m2}	W_{m1}	W_{m2}	h_{air}				
Value (mm)	0.65	0.2	0.4	1.7				

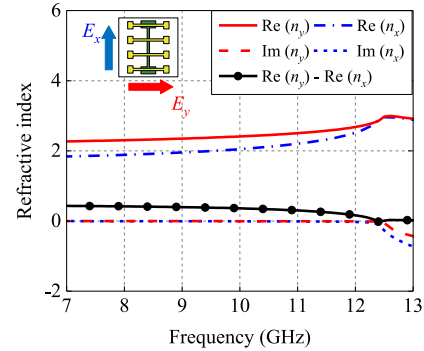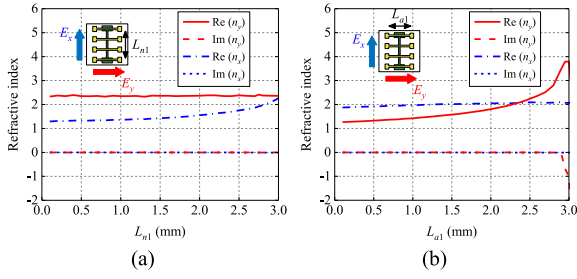FIGURE 16. Simulated refractive indexes for UC2 in two orthogonal polarizations.

of PCBs. Four horizontal H-shaped metallic strips along the y-axis are printed on the bottom of Layers 3 and 6, and top of Layers 5 and 8. A single vertical H-shaped metallic strip along the x-axis is printed between Layers 5 and 6. Fig. 13 shows the refractive indexes of UC1 for both x- and y- polarizations. It can be observed that because the variation of the refractive indexes in the x-polarization is larger than that of the indexes in the y-polarization, the difference of the refractive indexes for two polarizations decreases as the frequency increases, which fulfills the requirement of index variation for establishing a wideband polarizer as shown in Fig. 2. The refractive indexes in the x- and y-polarizations at 10 GHz with different L_{m1} and L_{c1} are simulated as shown in Fig. 14. When L_{m1} and L_{c1} are changed, other parameters are fixed. It is indicated that the refractive indexes in two polarizations can be tuned independently. The index in the x-polarization (n_x) varies from 2.1 to 3.8 by changing L_{m1} from 0.1 to 0.3 mm, while that in the y-polarization (n_y) varies from 2.1 to 6.88 by tuning L_{c1} from 0.1 to 2.95 mm. The independent control of refractive indexes in two polarizations enables tuning the index difference as required.

## B. IMPEDANCE MATCHING LAYER DESIGN AND ANALYSIS

According to (3), the required refractive index for IML is lower than that for the core layer so the height of IML is higher than the core layer. A dual-layer unit cell sandwiched with air layers is proposed to form the IMLs as shown in Fig. 15. Four horizontal H-shaped metallic strips along the y-axis are printed on top of Layer 1 and bottom of Layer 2. A single vertical H-shaped metallic strip along the x-axis is printed between Layers 1 and 2. Fig. 16 depicts the simulated refractive indexes versus frequencies for UC2 in both x- and y-polarizations. The refractive indexes in both polarizations are lower than those for the core layer, which meets the requirement for IML. The refractive indexes in the x- and y- polarizations for different values of L_{a1} and L_{n1} are carried out to demonstrate the characteristics of the proposed meta unit cell. As shown in Fig. 17 (a), when L_{n1} is tuned from 0.1 to 3 mm, the n_x varies from 1.2 to 2.25. Other parameters except for L_{n1} are fixed. Similarly, when

FIGURE 17. Simulated refractive indexes of UC2 for different values of (a) L_{n1} and (b) L_{a1}.
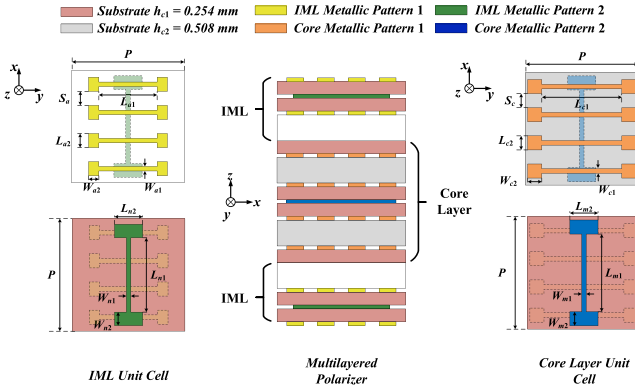
**FIGURE 18.** Geometry of the proposed multilayered wideband LP-CP polarizer.
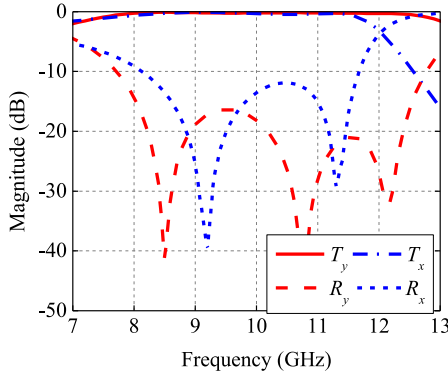
FIGURE 19. Simulated reflection coefficient (R_x and R_y) and transmission coefficient (T_x and T_y) of the proposed LP-CP polarizer.

L_{a1} is varied from 0.1 to 3 mm, the n_y changes from 1.2 to 3.8. Fig. 17 reveals that the refractive indexes in the x- and y-polarizations can be tuned by changing the parameters of L_{n1} and L_{a1} independently. This enables us to optimize the key parameters for achieving a wideband and low-loss polarizer.

C. OVERALL STRUCTURE DESIGN AND ANALYSIS

Based on the unit cell designs for the core layer and IML, a multilayered LP-CP polarizer is constructed by sandwiching UC1 with two UC2 as depicted in Fig. 18. All the parameters are optimized and provided in Table 4 in order to meet the requirements of composing a wideband LP-CP polarizer based on (1) to (4). To extract the reflection coefficient and
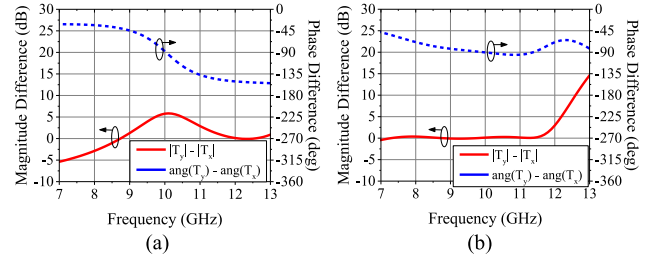
FIGURE 20. Simulated results of the transmission magnitude and phase for the proposed polarizer with (a) core layer only (b) core layer and IMLs.
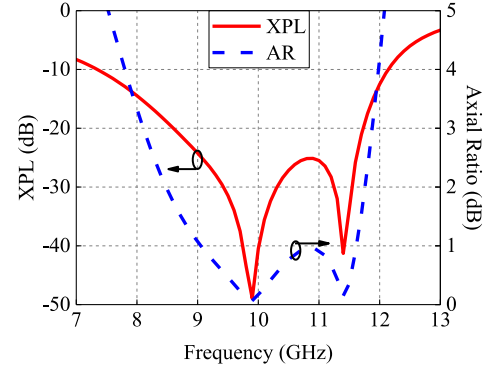

FIGURE 21. Simulated cross-polarization levels (XPL) and axial ratios (AR) of the proposed LP-CP polarizer.

transmission coefficient from the polarizer, the unit cell is simulated in the periodic boundary condition with the aid of the full-wave simulator HFSS.

The simulated reflection and transmission coefficients are shown in Fig. 19, which indicates that the reflection coefficients are below –10 dB, and the transmission coefficients are above –0.5 dB in frequencies ranging from 8.13 to 11.68 GHz for both polarizations. Furthermore, the effects of the IML on the transmission magnitude and phase of the proposed polarizer unit cell are depicted in Fig. 20. As shown in Fig. 20 (a), the polarizer utilizing the core layer only demonstrated the phase difference $\Delta\varphi = 90°$ at a single frequency point of 10 GHz and resulted in an unequal magnitude between the two orthogonal components over the bandwidth. While inserting the IML as a multilayer design, the consistent phase difference of 90 degrees and magnitude difference of 0 dB has been achieved for a wider bandwidth as illustrated in Fig. 20 (b). It can be claimed that the impedance matching layer is a crucial part of the design that affects and contributes to the AR bandwidth and impedance matching, and thus the proposed unit cell can meet the requirement for generating a CP wave.

Through the extracted transmission coefficients (T_x, T_y), the corresponding axial ratio and cross-polarization level can be derived from the scattering parameters. Accordingly, the cross-polarization levels (XPL) can be expressed with the commonly used formula,

$$XPL = \frac{|L|}{|R|} = \frac{|T_x - jT_y|}{|T_x + jT_y|} \qquad (5)$$
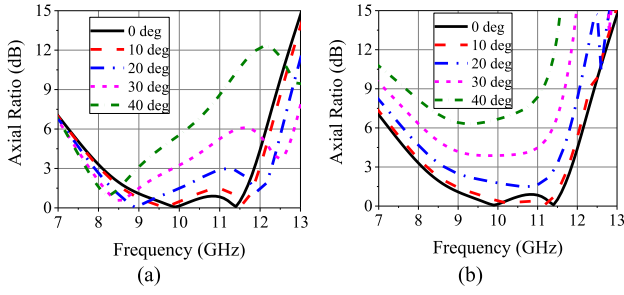
FIGURE 22. Axial ratio (AR) for different incident angles (θ) over the frequency range at (a) $\phi =0°$ (b) $\phi =90°$.

The axial ratio (AR) can be calculated as,

$$AR = \frac{|R| + |L|}{|R| - |L|} = \frac{|T_x + jT_y| + |T_x - jT_y|}{|T_x + jT_y| - |T_x - jT_y|} \quad (6)$$

where L and R are the left-handed and right-handed circular polarization phasors. Based on (5) to (6), the XPL and AR are calculated and depicted in Fig. 21. It can be found that the XPL is below -15 dB within frequencies ranging from 8.06 to 11.89 GHz while the 3-dB AR bandwidth is 8.11–11.88 GHz. The overlapped bandwidth of R_x, $R_y \leq -10$ dB, and AR ≤ 3 dB leads to the operating bandwidth of 8.13 GHz–11.68 GHz (35.8%). Moreover, the AR ≤ 1 dB bandwidth is 25%. The total thickness of the polarizer is 6.448 mm, which is 0.21 λ_0 where λ_0 is the wavelength of the center frequency at 10 GHz. The effect of the incident angle on AR bandwidth for each elevation plane is revealed in Fig. 22. The AR bandwidth is in descending order as the incident angle increases, while the polarizer works improperly when the incident angle exceeds $\theta = 20°$.

IV. PERFORMANCE OF THE LP-CP POLARIZER
A. FABRICATED PROTOTYPE
To validate the performance of the proposed design, the LP-CP polarizer consisting of 41*41 elements was fabricated and measured as shown in Fig. 23. Bonding films between the substrate layers and plastic screws on the substrate margin are added for ensuring seamless contact of the substrates and enhancing the robustness of the fabricated prototype. The selected bonding film, *Rogers 3001,* featured a low dielectric constant of $\varepsilon_r = 2.28$ and low loss tangent of $tan\delta = 0.03$ at the X-band frequency spectrum, and thus had minimum interference with the electrical performance of the multilayer construction. The effect of the bonding film on the AR and insertion loss (IL) are shown in Fig. 24. The 3dB AR bandwidth is slightly shifted to a higher frequency which may be related to the slight reduction of the proposed polarizer height, while there is no significant difference between the insertion losses of the polarizer with and without bonding film due to the comparable dielectric constant of the bonding film with air. Considering the alignment between the air gap and the substrate layers, the 3D-printed spacer with a precision of $\pm0.03mm$ is utilized on the margin of the substrate layer. Owing to the reinforced strength of the
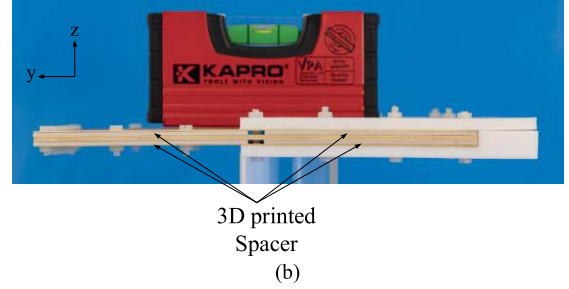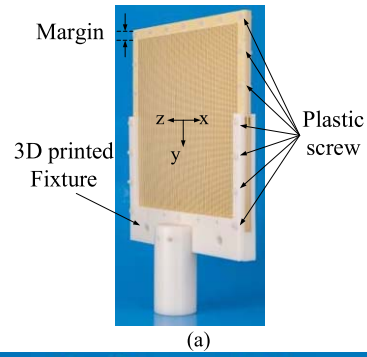
FIGURE 23. Fabricated prototype of the LP-CP polarizer measurement and actual measurement setup for prototype. (a) perspective view (b) side view.
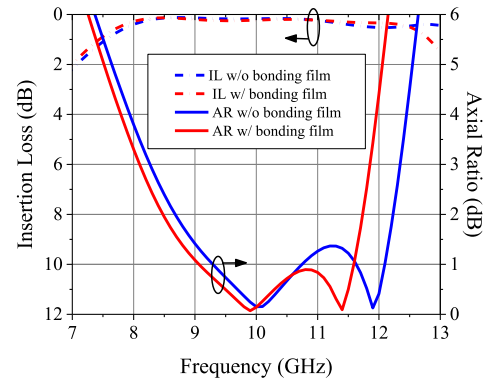
FIGURE 24. The effect of bonding film on the axial ratio and insertion loss of the proposed polarizer.

chosen substrate material, *Rogers 4003C,* the flatness of the fabricated prototype is promising with the consolidated multi-layered structure fastening with a significant amount of plastic screws.

B. MEASUREMENT SETUP AND RESULTS
Fig. 25 (a) displays the schematic diagram of the AR measurement setup while Fig. 25 (b) shows the actual measurement setup with the prototype of the proposed LP-CP polarizer. The proposed polarizer is fixed in the middle of the anechoic chamber with no mobility. For the transmission side, the *Narda model 640* standard gain horn with the aperture size D^2 of 78.49mm x 59.44mm is selected as the feeding horn and placed at the far-field distance $r = 2D^2/\lambda = 404$mm at 13 GHz. Meanwhile, an *NSI-RF-RGP40* double-ridged broadband horn antenna with an aperture size of 52mm x 44mm is deployed as the receiving horn and

(a)

(b)
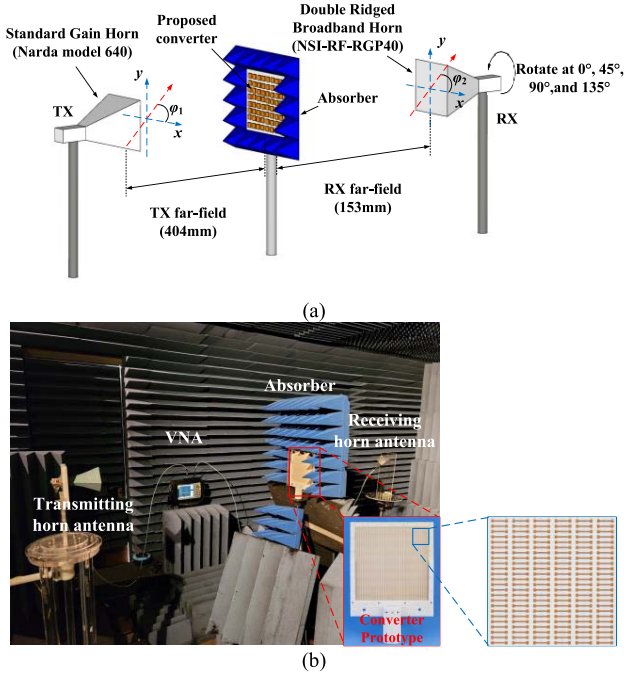
FIGURE 25. Schematic diagram of the LP-CP polarizer measurement and actual measurement setup for prototype. (a) Schematic diagram of the measurement. (b) Actual measurement setup with the photograph of the proposed prototype.

(a)

(b)

FIGURE 26. Measured results for the proposed LP-CP polarizer. (a) Measured S_{21} with the receiving antenna at φ_2=0°, 45°, 90°, and 135°. (b) Comparison of the insertion loss and AR between the simulation and measurement.

TABLE 5. Comparison of different LP-CP polarizers.

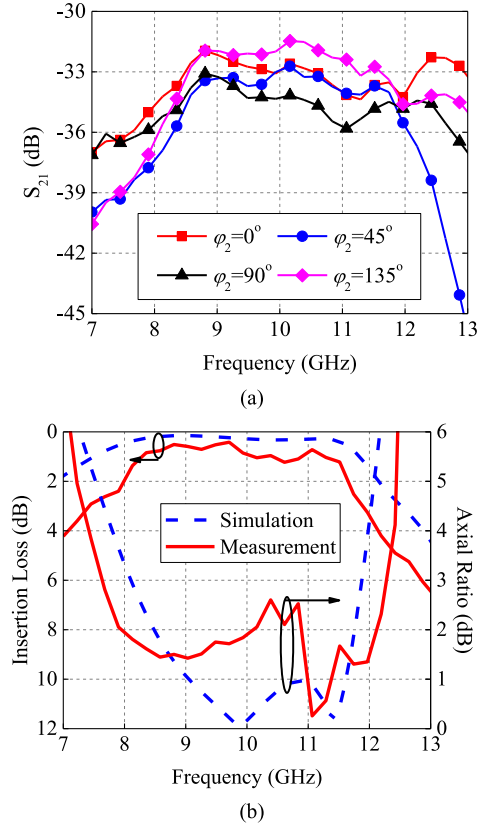| Design	Thickness	3-dB AR Bandwidth	Insertion Loss
[6]	0.48 λ_0	42%	1 dB
[13]	0.2 λ_0	25%	1.65 dB
[14]	0.725 λ_0	50%	1 dB
[17]	0.1 λ_0	17.5% (LHCP) 21.4% (RHCP)	1.8 dB (TE) 2.5 dB (TM)
[18]	0.18 λ_0	40%	3 dB
[20]	0.17 λ_0	64%	2 dB
[21]	0.27 λ_0	24%	1.1 dB
[26]	0.46 λ_0	42%	1 dB
[27]	0.23 λ_0	20%	0.6 dB
This work	0.21 λ_0	42%	1 dB

kept at a far-field distance of 198mm from the proposed polarizer. An *Anritsu MS2038C* VNA is adapted to connect the transmitting and receiving diagonal horn antennas. The transmitting horn antenna is aligned with the receiving one when the receiving one is rotated. The rotation angle φ_2 of the receiving antenna is at 0°, 45°, 90°, and 135° while φ_1 of the transmitting one is kept at 45°.

Fig. 26 (a) shows the measured S_{21} at the four rotation angles in the frequency ranging from 7 to 13 GHz. The measured AR can be obtained from the measured S_{21} at $\varphi_2 = 0°$, 45°, 90°, and 135° according to the equation [23], [24], [25],

$$AR = \sqrt{\frac{E_1^2 cos^2\tau + sin2\tau \left(E_3^2 - E_4^2\right)/2 + E_2^2 sin^2\tau}{E_1^2 sin^2\tau - sin2\tau \left(E_3^2 - E_4^2\right)/2 + E_2^2 cos^2\tau}} \quad (7)$$

where $\tau = 1/2 tan^{-1}[(E_3^2 - E_4^2)/(E_1^2 - E_2^2)]$, $E_1 = S_{21}(\varphi_2 = 0°)$, $E_2 = S_{21}(\varphi_2 = 90°)$, $E_3 = S_{21}(\varphi_2 = 45°)$, and $E_4 = S_{21}(\varphi_2 = 135°)$. The measured 3-dB AR bandwidth is 42% (7.9 – 12.2 GHz) as shown in Fig. 26 (b), which agrees well with the simulated one (8.1 – 11.8 GHz, 37%). The discrepancy between the simulated and measured AR may be caused by the misalignment between the transmitting and receiving horns at different rotation angles hence resulting in the inconsistency and variation of measured S_{21} at different rotation angles for AR calculation. However, the measured insertion loss ≤ 1 dB is within 8.2–11.8 GHz while the simulation value is lower than 0.5 dB. It is indicated that the working frequency band of the proposed design should be the overlapped bandwidth of 8.2 – 11.8 GHz.

Table 5 lists the performance of the proposed work compared with the polarizers proposed in the previous literature. Although the profile of the proposed design is higher than that in [13], [17], [18], and [20], the insertion loss of our design is much lower. For the low-insertion loss polarizers [6], [14], [21], [26], and [27], the proposed design takes advantage of low profile and wide bandwidth.

V. CONCLUSION
In this paper, a novel low-profile LP-CP polarizer based on anisotropic metamaterial has been investigated. It proposed a polarizer with independently controllable refractive indexes for two electric field components in orthogonal polarizations. Anisotropic meta unit cells are introduced to realize the

different refractive indexes in both polarizations and broaden the AR bandwidth. By inserting two impedance-matching layers, the impedance matching between the air and polarizer can be improved. As seen from the results, the polarizer exhibits a broadband characteristic with a wide 3-dB AR bandwidth of 42% ranging from 7.9 to 12.2 GHz. Moreover, the measured insertion loss within the operating bandwidth is smaller than 1 dB which is higher than that in simulation. Furthermore, the total thickness of the proposed polarizer is only 0.21 λ_0, which makes it a compact component for generating CP waves in high-speed communication, microwave imaging, and tracking systems.

REFERENCES

[1] D. Roddy, *Satellite Communications*, 4th ed. New York, NJ, USA: McGraw-Hill, 2006.

[2] C. Dietlein, A. Luukanen, Z. Popovic, and E. Grossman, "A W-band polarization converter and isolator," *IEEE Trans. Antennas Propag.*, vol. 55, no. 6, pp. 1804–1809, Jun. 2007.

[3] R. Orr, G. Goussetis, V. Fusco, and E. Saenz, "Linear-to-circular polarization reflector with transmission band," *IEEE Trans. Antennas Propag.*, vol. 63, no. 5, pp. 1949–1956, May 2015.

[4] K. X. Wang and H. Wong, "A wideband millimeter-wave circularly polarized antenna with 3-D printed polarizer," *IEEE Trans. Antennas Propag.*, vol. 65, no. 3, pp. 1038–1046, Mar. 2017.

[5] X. B. Zhao et al., "3-D printed conformal dielectric linear-to-circular polarization converters for cylindrical and spherical surfaces," *IEEE Antennas Wireless Propag. Lett.*, vol. 20, no. 12, pp. 2539–2543, Dec. 2021.

[6] H. Li, B. Li, and L. Zhu, "Wideband linear-to-circular polarizer based on orthogonally inserted slot-line structures," *IEEE Antennas Wireless Propag. Lett.*, vol. 18, pp. 1169–1173, 2019.

[7] Q.-W. Lin, S. Alkaraki, H. Wong, and J. R. Kelly, "A wideband circularly polarized antenna based on anisotropic metamaterial," *IEEE Trans. Antennas Propag.*, vol. 71, no. 2, pp. 1254–1262, Feb. 2023.

[8] R. Orr, G. Goussetis, and V. Fusco, "Design method for circularly polarized fabry–perot cavity antennas," *IEEE Trans. Antennas Propag.*, vol. 62, no. 1, pp. 19–26, Jan. 2014.

[9] L. Young, L. A. Robinson, and C. Hacking, "Meander-line polarizer," *IEEE Trans. Antennas Propag.*, vol. 21, no. 3, pp. 376–378, May 1973.

[10] R.-S. Chu and K.-M. Lee, "Analytical model of a multilayered meander-line polarizer plate with normal and oblique plane-wave incidence," *IEEE Trans. Antennas Propag.*, vol. 35, no. 6, pp. 652–661, Jun. 1987.

[11] M.-A. Joyal and J.-J. Laurin, "Analysis and design of thin circular polarizers based on meander lines," *IEEE Trans. Antennas Propag.*, vol. 60, no. 6, pp. 3007–3011, Jun. 2012.

[12] M.-A. Joyal, M. Riel, Y. Demers, and J.-J. Laurin, "A meander-line circular polarizer optimized for oblique incidence," *IEEE Trans. Antennas Propag.*, vol. 63, no. 12, pp. 5391–5398, Dec. 2015.

[13] F. A. Dicandia and S. Genovesi, "Linear-to-circular polarization transmission converter exploiting meandered metallic slots," *IEEE Antennas Wireless Propag. Lett.*, vol. 21, pp. 2191–2195, 2022.

[14] R. V. Gatti and R. Rossi, "A novel meander-line polarizer modeling procedure and broadband equivalent circuit," *IEEE Trans. Antennas Propag.*, vol. 65, no. 11, pp. 6179–6184, Nov. 2017.

[15] M. Euler, V. Fusco, R. Cahill, and R. Dickie, "325 GHz single layer sub-millimeter wave fss based split slot ring linear to circular polarization converter," *IEEE Trans. Antennas Propag.*, vol. 58, no. 7, pp. 2457–2459, Jul. 2010.

[16] M. Hosseini and S. V. Hum, "A semianalytical approach to designing high-transparency low-profile circular polarizers," *IEEE Trans. Antennas Propag.*, vol. 66, no. 12, pp. 7138–7147, Dec. 2018.

[17] F. Zhang, G.-M. Yang, and Y.-Q. Jin, "Design and analysis of linear to circular polarization converter with third-order meta-frequency selective surfaces," *IEEE Trans. Antennas Propag.*, vol. 68, no. 9, pp. 6646–6655, Sep. 2020

[18] S. M. A. M. H. Abadi and N. Behdad, "Wideband linear-to-circular polarization converters based on miniaturized-element frequency selective surfaces," *IEEE Trans. Antennas Propag.*, vol. 64, no. 2, pp. 525–534, Feb. 2016.

[19] L. Martinez-Lopez, J. Rodriguez-Cuevas, J. I. Martinez-Lopez, and A. E. Martynyuk, "A multilayer circular polarizer based on bisected split-ring frequency selective surfaces," *IEEE Antennas Wireless Propag. Lett.*, vol. 13, pp. 153–156, 2014.

[20] W. Zhang, J. Li, and J. Xie, "A broadband circular polarizer based on cross-shaped composite frequency selective surfaces," *IEEE Trans. Antennas Propag.*, vol. 65, no. 10, pp. 5623–5627, Oct. 2017.

[21] E. Arnieri, F. Greco, and G. Amendola, "A broadband, wide-angle scanning, linear-to-circular polarization converter based on standard jerusalem cross frequency selective surfaces," *IEEE Trans. Antennas Propag.*, vol. 69, no. 1, pp. 578–583, Jan. 2021.

[22] Q.-W. Lin and H. Wong, "A low-profile and wideband lens antenna based on high-refractive-index metasurface," *IEEE Trans. Antennas Propag.*, vol. 66, no. 11, pp. 5764–5772, Nov. 2018.

[23] G. E. Evans *Antenna Measurement Techniques* Norwood, MA, USA: Artech House, 1990.

[24] B. Y. Toh, R. Cahill, and V. F. Fusco, "Understanding and measuring circular polarization," *IEEE Trans. Educ.*, vol. 46, no. 3, pp. 313–319, Aug. 2003.

[25] B. Li, Y.-S. Zeng, B.-J. Chen, and C. H. Chan, "Terahertz frequency-selective surface with polarization selection and conversion characteristics," *IEEE Trans. Thz Sci. Technol.*, vol. 9, no. 5, pp. 510–519, Sep. 2019.

[26] M. Akbari, M. Farahani, A.-R. Sebak, and T. A. Denidni, "Ka-band linear to circular polarization converter based on multilayer slab with broadband performance," *IEEE Access*, vol. 5, pp. 17927–17937, 2017.

[27] M. Hosseini and S. V. Hum, "A circuit-driven design methodology for a circular polarizer based on modified jerusalem cross grids," *IEEE Trans. Antennas Propag.*, vol. 65, no. 10, pp. 5322–5331, Oct. 2017.

YAT SING TO (Graduate Student Member, IEEE) received the B.Eng. degree in electronic engineering from the City University of Hong Kong, Hong Kong, in 2020, where he is currently pursuing the Ph.D. degree in the field of electrical engineering.

His current research interests include the design of millimeter-wave and terahertz antennas, reconfigurable antennas, meta-material/surface, and functional-material antennas. He was the recipient of the Third Prize in the Student Paper Competition of the 21st IEEE (HK) AP/MTT Postgraduate Conference in 2020, the Awardee of the Hong Kong Ph.D. Fellowship Scheme in 2020, and the Best Paper Award in the 24th IEEE (HK/GZ) AP/MTT Postgraduate Conference in 2023.

XUE REN (Member, IEEE) received the Ph.D. degree in electrical engineering from the State Key Laboratory of Terahertz and Millimeter Waves, City University of Hong Kong (CityU), Hong Kong, in 2020, where he was a Research Assistant with the Shenzhen Key Laboratory of MWWC, Shenzhen Research Institute from 2015 to 2016. He is currently an Assistant Professor with the College of Electronics and Information Engineering, Shenzhen University, Shenzhen, China. His current research interests include beamforming antennas, satellite antennas, metamaterials, millimeter-wave antennas, array technology, and RF front-end circuits. He was a recipient of the Outstanding Academic Performance Award from CityU in 2018 and 2019. He also serves as a Reviewer for several technique journals, including IEEE TRANSACTIONS ON ANTENNAS AND PROPAGATION and the IEEE ANTENNAS AND WIRELESS PROPAGATION LETTERS. He was a TPC Member of the Cross Strait Radio Science and Wireless Technology Conference 2021, Shenzhen, China, and the IEEE MTT-S International Microwave Workshop Series on Advanced Materials and Processes for RF and THz Applications in 2022.

QUAN-WEI LIN (Member, IEEE) was born in Xinhui, Guangdong, China. He received the B.E. degree in information engineering and the M.E. degree in communication and information systems, from the South China University of Technology, Guangzhou, China, in 2013 and 2016, respectively, and the Ph.D. degree in electrical engineering from the City University of Hong Kong, Hong Kong, in 2019.

He joined the State Key Laboratory of Terahertz and Millimeter Waves, City University of Hong Kong as a Postdoctoral Fellow in 2019. He has published more than 30 international journals and conference papers. He was awarded four China patents. His current research interests include millimeter-wave antennas, metasurfaces, and reconfigurable reflectarrays.

Dr. Lin was a recipient of the Third Prize in the Student Innovation Competition of the 2013 IEEE International Workshop on Electromagnetics.

HANG WONG (Senior Member, IEEE) received the B.Eng., M.Phil., and Ph.D. degrees in electronic engineering from the City University of Hong Kong in 1999, 2002, and 2006, respectively. He joined the Department of Electrical Engineering, City University of Hong Kong in 2012. He had several visiting professorships with Stanford University, USA; the University of Waterloo, Canada; the University of College London, U.K.; and the University of Limoges, France, in the years of 2011, 2013, 2014, and 2015 respectively. He is the Director of the Applied Electromagnetics Laboratory, CityU; and the Deputy Director of the State Key Laboratory of Terahertz and Millimeter Waves, Hong Kong. His research interests are antenna technologies of 5G, 6G, millimeter-wave and terahertz applications. He has over 200 publications, two coauthors of book chapters and 20 U.S. and China patents. His achievements led to receiving numerous awards at local, national and international conferences. For example, he received the Best Paper Award at the National Conference 2017 Les Journées Nationales Microondes in France; the Best Paper Award at the 2017 IEEE International Workshop on Electromagnetics in the U.K.; the Best Associate Editor Award 2016 of an IEEE ANTENNAS AND WIRELESS PROPAGATION LETTERS in the U.S.; and an Outstanding Scientist Award of 2016 in Shenzhen City presented by Shenzhen Science and Technology Bureau. He was awarded to lead a major project supported by the Ministry of Industry and Information Technology of PRC to develop new antenna elements for TD-LTE and 5G applications. He is the Chair of the IEEE Hong Kong Section of the Antennas and Propagation/Microwave Theory and Techniques Chapter. He is an Associate Editor of IEEE TRANSACTIONS ON ANTENNAS AND PROPAGATION and IEEE ANTENNAS AND WIRELESS PROPAGATION LETTERS. He was the IEEE APS Region-10 Representative. He was the General Co-Chair of the Asia–Pacific Microwave Conference 2020, Hong Kong; and the General Chair of Cross-Strait Radio Science and Wireless Technology Conference 2021, Shenzhen, China.